GlobULeS. IV. UVIT/AstroSat Detection of Extremely Low Mass White Dwarf Companions to Blue Straggler Stars in NGC 362

Arvind K. Dattatrey[1,2] , R. K. S. Yadav[1], Sharmila Rani[3] , Annapurni Subramaniam[3] , Gaurav Singh[3], Snehalata Sahu[4], and Ravi S. Singh[2]

[1] Aryabhatta Research Institute of Observational Sciences, Manora Peak, Nainital 263002, India; arvind@aries.res.in, rkant@aries.res.in
[2] Deen Dayal Upadhyay Gorakhpur University, Gorakhpur, Uttar Pradesh 273009, India
[3] Indian Institute of Astrophysics, Koramangala, Bangalore 560034, India; purni@iiap.res.in, sharmila.rani@iiap.res.in
[4] University of Warwick, Coventry CV4 7AL, UK
Received 2022 November 15; revised 2022 December 19; accepted 2022 December 19; published 2023 February 2

Abstract

We report the discovery of extremely low mass white dwarfs (ELM WDs) as a companion of blue straggler stars (BSSs) in the Galactic globular cluster NGC 362 using images from AstroSat's Ultra Violet Imaging Telescope (UVIT). Spectral energy distributions (SEDs) for 26 far-UV (FUV) bright member BSSs are created using data from the UVIT, the UltraViolet and Optical Telescope (UVOT), Gaia EDR3, and the 2.2 m ESO/MPI telescope. A single SED is fitted to 14 BSSs, whereas double-SED fits revealed ELM WDs as binary companions in 12 of the 26 BSSs studied. The effective temperature, radius, luminosity, and mass of the 12 ELM WDs are found to have a range of $T_{\rm eff} = 9750-18,000$ K, $R = 0.1-0.4\,R_{\odot}$, $L = 0.4-3.3\,L_{\odot}$, and $M = 0.16-0.20\,M_{\odot}$. These suggest that 12 BSSs are post-mass-transfer systems formed through the case A/B mass transfer pathway. To the best of our knowledge, this is the first finding of ELM WDs as companions to BSSs in globular clusters. This cluster is known to have a binary BSS sequence, and the 12 binary and 14 single BSSs (as classified by the SEDs) follow the mass transfer and collisional sequence of BSSs in the color–magnitude diagram. The cooling ages of nine of the ELM WDs are found to be younger than 500 Myr. Though the binary BSSs may have formed during the core collapse (∼200 Myr) or as part of the dynamical evolution of the cluster, they provide new insights on the dynamics of this cluster.

Unified Astronomy Thesaurus concepts: Ultraviolet astronomy (1736)

1. Introduction

Globular clusters (GCs) are one of the oldest stellar systems in which frequent gravitational interactions among stars take place owing to their high densities. These gravitational interactions lead to several dynamical processes, i.e., two-body relaxation, mass segregation from equipartition of energy (Lanzoni et al. 2007; Martinazzi et al. 2014; Baumgardt 2017), core collapse (Meylan & Heggie 1997), stellar collisions, and mass transfers (MTs) and mergers (Kravtsov et al. 2022) in binary star systems. These dynamical processes produce exotic populations like low-mass millisecond pulsars (MSPs), cataclysmic variables, and blue straggler stars (BSSs). BSSs are found in bulk among these exotic populations (Bailyn & Pinsonneault 1995; Ferraro et al. 2001).

BSSs were first discovered by Sandage (1953) in the outskirts of GC M3, where they appear as an extension of the main sequence (MS) in the optical color–magnitude diagram (CMD). They are generally found in diverse stellar environments such as GCs (Sandage 1953; Ferraro et al. 1993), open clusters (OCs; Johnson & Sandage 1955), dwarf galaxies (Clarkson et al. 2011), and galactic fields (Preston & Sneden 2000). Several observational evidences (Renzini & Fusi Pecci 1988; Shara et al. 1997) suggest that BSSs are more massive $(M \sim 1.2\,M_{\odot})$ than the typical turnoff stars $(M \sim 0.95\,M_{\odot})$ in GCs.

The formation of BSSs cannot be explained through canonical stellar evolution theory. Therefore, their formation must be looked into by some mechanisms that are able to increase the initial mass of single stars (Ferraro et al. 2018). The formation mechanism of BSSs is still being debated. However, the two leading formation mechanisms of BSSs are as follows. The first mechanism is that of stellar collisions (Hills Day 1976; Leonard 1989) that lead to a merger in high-density environments and MT (McCrea 1964; Zinn & Searle 1976) from an evolved donor to a lower-mass binary star in a low-density environment. Another mechanism for twin BSS formation in a compact binary system has been proposed by Portegies Zwart & Leigh (2019), in which mass is transferred through a circumbinary disk from an evolved outer tertiary companion.

Depending on the evolutionary type of the donor star, three distinct scenarios of MT have been presented (Kippenhahn et al. 1967; Paczyński 1971) for the formation of BSSs through Roche lobe (RL) overflow. They are as follows: case A—an MS star; case B—a red giant branch (RGB) star; case C—an asymptotic giant branch (AGB) star. In case A, an MT can result in the production of either a single BSS or short-period binary BSSs, whereas BSSs with a white dwarf (WD) companion having either He or CO core of masses 0.2–0.4 $M_{\odot}$ and 0.5–0.6 $M_{\odot}$, respectively, are produced through case B and case C (Perets & Fabrycky 2009).

Extremely low mass (ELM) helium WDs have effective temperatures in the 8000 K $\leqslant T_{\rm eff} \leqslant$ 22,000 K range and masses of less than 0.3 $M_{\odot}$. They are most likely the result of binary interactions (Marsh et al. 1995). These low-mass stellar objects cannot be formed from single-star progenitors because

their nuclear evolution timescale exceeds the Hubble time unless they have extremely high metallicity (Kilic et al. 2007). Hence, the majority of these objects are found in binary systems with companions such as neutron stars in MSP systems (van Kerkwijk et al. 2005), A/F-type dwarf stars (Maxted et al. 2014), or another (typically a carbon–oxygen) WD. These objects can be found in a variety of environments, including the Galactic disk, OCs, and GCs (Rivera-Sandoval et al. 2015). Hence, they can be formed from progenitors of varying metallicities. These WDs are believed to be originated through either unstable mass loss via common envelope (CE) events or stable mass loss via RL overflow in close binary systems with a thick envelope (Althaus et al. 2013).

In the CE model, the secondary component fills the RL during the Hertzsprung gap or near the RGB phase, leading to an unstable MT. Such a state evolves into a new CE state, where the system eventually evolves into a double-degenerate (DD) binary. The ELM WDs with masses $\leqslant 0.2\,M_\odot$ cannot be produced through the CE scenario since the high binding energy of the CE in such a binary system could lead to a merger rather than an ejection during the CE evolution. In contrast, in the RL model, the secondary component initiates a stable MT during late MS, leading to the formation of a proto-He WD. The system then progresses to a DD binary with an ELM WD mass ranging from 0.14 to $0.30\,M_\odot$.

Dalessandro et al. (2013, hereafter D13) identified two distinct BSS sequences in the post-core-collapse GC NGC 362. They suggested that this feature is caused by short-duration dynamical events in the cluster, such as core collapse. Similarly, the double sequences of BSSs have been found in several GCs, including M30 (Ferraro et al. 2009), NGC 1261 (Simunovic et al. 2014), and M15 (Beccari et al. 2019). The bluer BSS sequence is thought to be formed by the increased star collision rate during core contraction, while the redder BSS sequence is caused by the increased RL overflows.

UV observations are crucial to identify and understand the nature of the companion to the BSSs. BSSs define a clear vertical sequence in the UV CMD (Siegel et al. 2014; Ferraro et al. 2018). In particular, ASTROSAT/Ultra Violet Imaging Telescope (UVIT) data have been extensively used to characterize BSSs and identify their hot companions based on UV excess. Subramaniam et al. (2016a) discovered a post-AGB/horizontal branch (HB) companion of a BSS in the old OC NGC 188 utilizing UVIT data. Sindhu et al. (2019), Pandey et al. (2021), and Jadhav et al. (2021) used UVIT data to analyze OCs and found BSSs with hot companions. In GC NGC 1851, Singh et al. (2020) discovered extreme HB (EHB) stars as hot companions to the BSS.

This paper presents the UV photometric results of GC NGC 362 located in the southern hemisphere of the Tucana constellation and slightly northward of the Small Magellanic Cloud (SMC). The age of the cluster is ~11 Gyr, located at a distance of ~8.83 kpc (Vasiliev & Baumgardt 2021), with a reddening ~0.05 mag (Harris 2010) and a metallicity of [Fe/H] ~−1.3 dex. The tidal radius (r_t) of the cluster is $r \sim 16'.11$. This cluster has been extensively studied in the optical region, but UV study is limited. Our main aim in this study is to characterize the BSS population primarily using data from UVIT on board AstroSat to shed more light on their nature, as well as formation scenarios of BSSs in GC NGC 362.

This paper is organized as follows. Section 2 covers the archival/observational data, along with their reduction and analysis methods. In Section 3, we present the details of the UV and optical CMDs, as well as the selection of BSSs. The details of the SED fitting technique are described in Section 4. We discuss the properties of BSSs derived using the SED technique and their evolutionary status in Section 5. A detailed discussion of all the results is presented in Section 6, followed by the summary and conclusions in Section 7.

2. Data Sets and Their Reduction

In order to study the BSS population in NGC 362, we have utilized the multiwavelength data from several telescopes covering the entire cluster region up to r_t. We have used the UVIT, UltraViolet and Optical Telescope (UVOT), and 2.2 m MPI/ESO observations for this analysis. The details of the data used and their reductions are as follows.

UVIT.—We used images of NGC 362 captured by the UVIT instrument on board the AstroSat satellite. UVIT is made up of two 38 cm telescopes, one for the far-UV (FUV) region (130–180 nm) and another for the near-UV (NUV; 200–300 nm) and visible (VIS; 320–550 nm) regions. The cluster's level 1 data were acquired from the AstroSat archive.[5] The observations of NGC 362 were carried out on 2016 November 11 in four UV filters: F148W, F169M, N245M, and N263M. The exposure time and filter information are provided in Table 1. Data reduction of the raw images was performed using CCDLAB (Postma & Leahy 2017), which corrects the satellite drift, flat-field, distortion, fixed pattern noise, and cosmic rays. The detailed descriptions of the telescope, instruments, and preliminary calibration can be found in Subramaniam et al. (2016b) and Tandon et al. (2017).

The point-spread function (PSF) photometry was performed on all UVIT images using DAOPHOT II (Stetson 1987) programs. The ALLSTAR program was then used to fit the PSF model to the aperture magnitudes of all known stars. The aperture correction was established in each filter using a curve-of-growth analysis and then applied to the estimated PSF magnitudes. The saturation correction (Tandon et al. 2017) was applied to the PSF-generated magnitude to account for more than one photon per frame, yielding the instrumental magnitudes. Stars brighter than 17 mag are affected mainly by saturation correction. The zero-points are used from Tandon et al. (2017) to determine the magnitudes in the AB system. The astrometry of the UVIT images was performed using the WCS task in CCDLAB software (Postma & Leahy 2017) by utilizing the sky coordinate information from Gaia eDR3.

UVOT.—The raw data obtained from the HEASARC archive[6] have been processed using the HEASoft[7] pipeline. The log of observations is given in Table 1. The corrections were applied for exposure maps and auxiliary spacecraft data, and the science images were geometrically corrected for sky coordinates. The procedure described in Siegel et al. (2014) was followed to reduce the UVOT/Swift data. The large-scale sensitivity (LSS) maps for individual frames were generated using the UVOTSKYLSS task. These frames were combined into a single multi-extension file using the FAPPEND task. UVOTIMSUM generated a single image for each filter and their corresponding sensitivity and exposure map images.

---

[5] https://astrobrowse.issdc.gov.in/astroarchive/archive/Home.jsp
[6] https://heasarc.gsfc.nasa.gov
[7] https://heasarc.gsfc.nasa.gov/docs/software/heasoft

Table 1
Log of Archival Data

Telescopes	Filters	FOV	Exposure Time (ks)
HST	F275W, F336W, F438W (WFC3/UVIS)	$160'' \times 160''$	3.1, 1.4, 0.2
	F606W, F814W(ACS/WFC)	$202'' \times 202''$	0.6, 0.6
UVIT/AstroSat	F148W, F169M, N245M, N263M	$28'$	4.9, 4.6, 4.9, 4.6
UVOT/Swift	uvw2(192 nm), uvm2(224 nm), uvw1(260 nm)	$17' \times 17'$	2.4, 1.7, 1.7
2.2 m MPI/ESO	U, B, V, R, I	$34' \times 33'$	0.24, 0.24, 0.09, 0.045, 0.045

The PSF photometry on all UVOT images (uvw1, uvm2, and uvw2 filters) was performed using DAOPHOT II (Stetson 1987) programs. We performed aperture photometry with a $5''\!.0$ aperture radius to figure out the aperture correction. Singh et al. (2020) discussed the reduction and calibration of UVOT images in detail.

2.2 m ESO/MPI.—The archival images obtained by the Wide-Field Imager (WFI) placed on the 2.2 m ESO/MPI ground-based telescope were used to investigate the outer region of NGC 362. The broadband U, B, V, R, and I filters are used. The observational log of the archival data is provided in Table 1. With a total field of view (FOV) of $34' \times 33'$, the WFI is composed of eight CCDs (each with 2048×4096 pixels with a size of $0''\!.238$ pixel^{-1}). The raw science images were preprocessed using the MSCRED package available in IRAF.

The photometry on the WFI images was performed following the approach described in A06 (Anderson et al. 2006). The PSF's shape varies greatly with position; hence, nine PSFs per CCD chip (3×3) were developed to limit spatial fluctuation to less than 1% (Singh & Yadav 2018). The PSFs were developed using an empirical grid with a quarter-pixel resolution. Each PSF was represented by a 201×201 grid with a radius of 25 pixels and a center (101, 101). An automated code (Anderson et al. 2006) was used to interactively find the instrumental magnitudes and positions using the array of generated PSFs. The code first detects the brightest stars and then moves to the fainter stars. The distortion solution derived in A06 was used to minimize the effect of geometric distortion. The B, V, R, and I instrumental magnitudes were converted to the standard magnitude using the Stetson (Stetson et al. 2019) photometric standard. The image coordinates of WFI and UVOT images were converted into sky coordinates using the CCMAP and CCTRAN tasks of IRAF. The astrometric accuracy of all the images was $\sim 0''\!.1$.

Apart from the above data, we also have used Hubble Space Telescope (HST) data covering the central region ($r \leqslant 90''$) of the cluster, as it is an ideal instrument to resolve the core of the clusters. The HST UV Legacy Survey of Galactic Globular Clusters (HUGS) catalog was used, which comprises photometric magnitudes in five filters, namely, F275W, F336W, F438W, F606W, and F814W, along with proper-motion membership information (Nardiello et al. 2018).

3. UV and Optical Color–Magnitude Diagrams

In this section, we present the details of data cross-match and selection of BSSs using optical and UV CMDs. The UVIT data were combined with UV–optical astro-photometric data from HST, UVOT, 2.2 m ESO/MPI, and Gaia EDR3. The matched UV–optical data were analyzed using the UV–optical CMDs for selecting BSSs.

3.1. Cross-match of UV Data with Optical Data

Our main focus in this paper is to study the UV-bright BSSs detected in the FUV images. For this purpose, we first identified the FUV-bright BSSs in the inner region ($r \leqslant 90''$) by cross-matching UVIT and HST photometric data with matching radius $1''$. For identifying the FUV-bright BSSs in the outer region ($90'' < r < r_t$), we cross-matched the UVIT data with the UVOT/Swift and 2.2 m ESO/MPI photometric data with matching radius $1''\!.5$. We used the membership probability information provided in the GlobULeS I catalog (Sahu et al. 2022) for the outer region. Stars having a membership probability greater than 90% were chosen to be cluster members and considered for further analysis.

3.2. Selection of Blue Straggler Stars

Using optical counterparts of the UVIT detected sources in NGC 362, we constructed UV–optical CMDs of members for the inner and outer regions. The CMDs are a vital tool to identify stars at various stages of evolution in clusters. Both UV and optical CMDs can be used to select the BSSs in star clusters, but UV CMDs are preferred over optical CMDs, as BSSs appear brighter in them and also can be easily separated from the hot HB stars (Raso et al. 2017) and stars near the MS turnoff.

In Figure 1, we plotted NUV CMD (m_{F275W}, $m_{F275W} - m_{F336W}$) using the HST catalog. For the outer region, we created the optical CMD (G, $G_{BP} - G_{RP}$) using the Gaia eDR3 photometric catalog as shown in Figure 2. In both CMDs, circles represent stars with a membership probability greater than 90%.

The BSSs were chosen using the method described in Raso et al. (2017), with UV CMD provided as the main selection criterion. To select the BSS in both the inner and outer regions of the cluster, we drew a box around the BSS sequence in the CMDs presented in Figures 1 and 2. We defined the fainter limit of the box in Figure 1 as 5σ above the MS turnoff. By averaging the magnitudes and colors of stars in a box of 1 mag near the turnoff point on the MS, σ was calculated. In this way, a total of 48 BSSs were identified in the inner region. A similar box was also drawn in Figure 2 to pick out the BSSs in the outer region. We found 20 BSSs in the outer region. In total, 68 BSSs (48 in the inner region and 20 in the outer region) were identified in the cluster NGC 362 and are depicted with blue filled circles in Figures 1 and 2.

To clearly distinguish and select the FUV-bright BSSs, we plotted the FUV–optical CMD (F148W, F148W−G) shown in Figure 3. The red filled circles represent the HB stars, while the filled and open blue symbols represent the BSSs for the inner and outer regions, respectively. In this way, we selected 26 FUV-bright BSSs. We also plotted the updated BaSTI
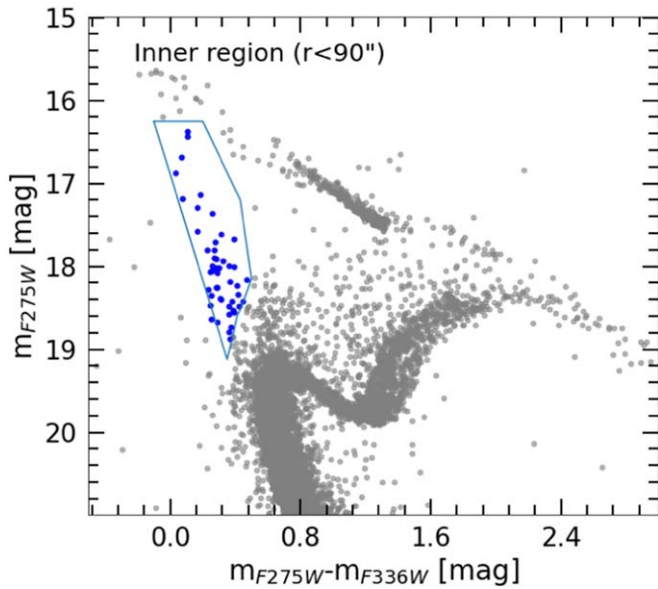
Figure 1. The selection criterion for the BSSs in UV CMD (m_{F275W}, $m_{F275W}-m_{F336W}$) for the inner region is shown with the box. The selected BSSs are shown with filled blue circles.
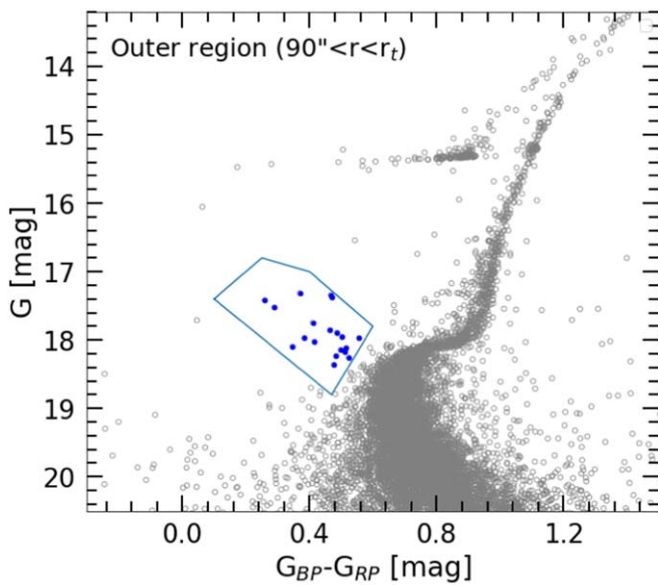

Figure 2. The selection criterion for the BSSs in optical CMD (G, $G_{BP} - G_{RP}$) for the outer region is shown with the box. The selected BSSs are shown with the filled blue circles.

Figure 3. The F148W vs. F148W$-G$ CMD of hot populations. The UVIT-Gaia EDR3 cross-matched sources are plotted. The reddening and distance modulus of the cluster are taken from Harris (2010). The models of ZAMS, ZAHB, and TAHB taken from the BaSTI-IAC online database (Hidalgo et al. 2018; Pietrinferni et al. 2021) are overplotted.

4. Spectral Energy Distribution of the FUV-bright BSSs

A detailed SED analysis was performed to evaluate the fundamental parameters of the FUV-bright BSSs, such as their total luminosity ($L/L_\odot$), effective temperature (T_{eff}), and radius ($R/R_\odot$). The SED was created using photometric data ranging from UV to IR wavelengths for the 26 FUV-bright BSS candidates. SED analysis was carried out using the Virtual Observatory SED Analyzer (VOSA; Rodrigo et al. 2019).

To correct for extinction in the observed data points, VOSA employs the reddening relations provided by Fitzpatrick (1999) and Indebetouw et al. (2005). The extinction-corrected VOSA magnitudes agree with those calculated by us. The VOSA performs a reduced χ^2 (χ_r^2) minimization test by comparing synthetic photometry to observed data to determine the best-fit SED parameters. Subramaniam et al. (2016a) and Rani et al. (2021) describe the detailed procedure for analyzing SEDs. VOSA provides two more characteristic parameters, Vgf and Vgf_b, in addition to χ_r^2, which are referred to as visual goodness of fit. Vgf and Vgf_b should be less than 25 and 15, respectively (Jiménez-Esteban et al. 2018; Rebassa-Mansergas et al. 2021), for the best fit. VOSA estimates the uncertainties in the derived parameters using the Markov Chain Monte Carlo technique.

The Kurucz stellar atmospheric models were used to generate synthetic SEDs for the FUV-bright BSSs (Castelli et al. 1997; Castelli & Kurucz 2003). The effective temperatures were chosen to be between 5000 and 50,000 K, with a metallicity value of [Fe/H] = -1 close to the cluster metallicity, and a corresponding log g ranging from 3 to 5 dex. For the SED analysis of FUV BSSs, the UVIT data were combined with HST data for the inner region and with UVOT and Gaia data for the outer region.

First, we fitted a single-component SED to the 26 FUV-bright BSSs with the Kurucz stellar atmospheric model as shown in the top panel of Figures 5 and 6. The data points used

isochrone[8] (Hidalgo et al. 2018; Pietrinferni et al. 2021) models of zero-age MS (ZAMS), zero-age HB (ZAHB), and terminal-age HB (TAHB) in the CMD with dashed–dotted, solid, and dashed lines, respectively. These isochrones are corrected for reddening and extinction (Fitzpatrick 1999; Chen et al. 2019). Both HB and BSS sequences can be clearly seen in Figure 3. The BSS sequence is ~4 mag, while the HB sequence is ~5 mag, stretched along the F148W magnitude axis. All these FUV-bright BSSs are clearly resolved, as shown in Figure 4.
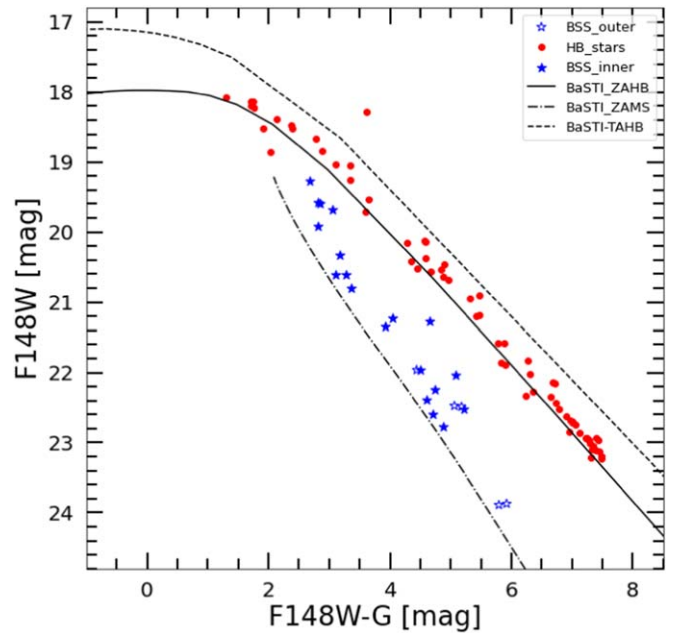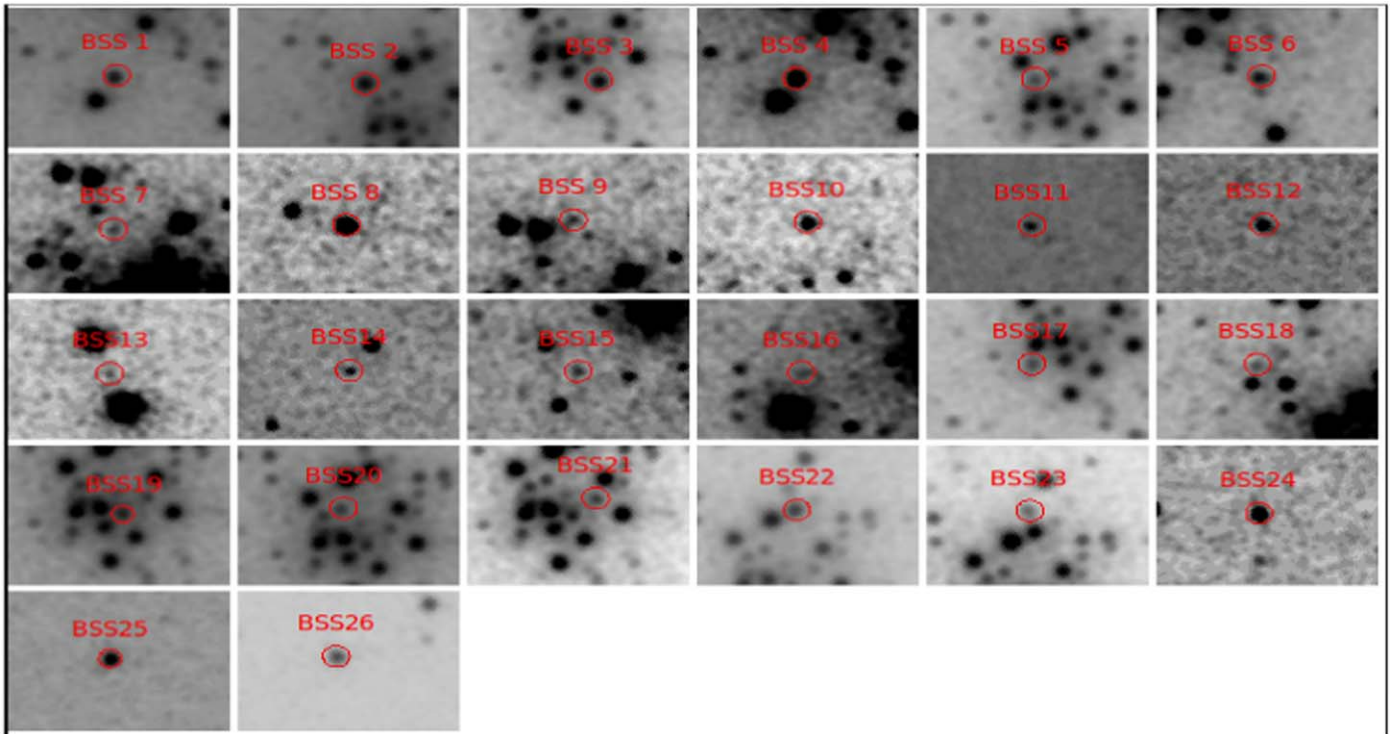
---

[8] http://basti-iac.oa-abruzzo.inaf.it

Figure 4. The location of FUV-bright BSSs in the FUV (F148W) image of UVIT. Each image has an FOV of $40'' \times 30''$.

in the fitting are shown as red, cyan, and orange-red filled circles with error bars, while model data points are shown as blue points. The Kurucz spectra are depicted with a gray line. The residual between the fitted model and the observed fluxes normalized by the observed flux across all filters is shown in the lower panel of each SED. The residual points with the error are represented by sky-blue filled circles. The dashed horizontal lines drawn at ± 0.3 (30%) represent the residual's threshold. The residual plots presented in Figure 5 show that the residuals for the 14 BSSs (BSS01–BSS14) are within 0.3 across all wavelengths. This indicates that the single-component Kurucz model fits these 14 BSSs well.

To determine the fundamental parameters of the 14 BSSs (Group 1), VOSA uses χ_r^2 fitting. Table 2 shows the effective temperature, log g, luminosity, and radius, along with the χ_r^2 for the single-component BSSs. The ranges in different parameters are found as $T_{\rm eff} \sim 7500$–9250 K, log $g \sim 4.0$–5.0, $L \sim 4.3$–19.1 $L_\odot$, and $R \sim 1.1$–2.0 $R_\odot$. We can see that estimated parameters are consistent with the BSS properties (Subramaniam et al. 2016a; Rani et al. 2021).

Figure 6 shows the best SED fits for the 12 BSSs (BSS15–BSS26). The Kurucz model is shown with a gray solid line. The residual plot for the 12 BSSs (Group 2) shows that the residual flux in the UV region is greater than 0.3 in more than one data point. This indicates that there is UV excess, and the SEDs may be fitted by a combination of hotter and cooler spectra.

4.1. The Two-component SED Fits

To account for the UV excess in the BSS of Group 2, we fitted two-component SEDs as shown in Figure 6. We used the Kurucz stellar atmospheric model (Castelli et al. 1997; Castelli & Kurucz 2003) to fit for the cooler component and the Koester WD model (Koester 2010) to fit for the hotter component. In the Koester WD model, $T_{\rm eff}$ and log g are in the range of 5000 −80,000 K and 6.5−9.5, respectively.

In the top panel, observed data points are indicated with red filled circles, while synthetic data points are shown with blue filled circles. The cool and hot synthetic spectra are represented by gray and black lines, respectively. We used VOSA to get the two-component fit of these stars.[9] The composite SEDs are shown in black in Figure 6. We can see that the composite SEDs are well fitted across all wavelengths. The hot components are well fitted with a Koester model, whereas the cool components are well fitted with a Kurucz model. In the bottom panel of each SED, the fractional residuals are plotted with sky-blue points. The fractional residuals are within ± 0.3 (30%) across all wavelengths.

The fundamental parameters of these BSSs derived using composite SED fits are listed in Table 3. The ranges in parameters for cool companions are $T_{\rm eff} \sim 6200$–8250 K, log $g \sim 3.5$–5.0, $L \sim 2.3$–14.9 $L_\odot$, and $R \sim 1.0$–2.1 $R_\odot$, and those for hot companions are $T_{\rm eff} \sim 9750$–18,000 K, log $g = 6.5$–7.75, $L \sim 0.4$–3.3 $L_\odot$, and $R \sim 0.1$–0.4 $R_\odot$. The goodness-of-fit parameters, i.e., χ_r^2, Vgf, and Vgf$_b$, are also listed in Table 3. Based on their $T_{\rm eff}$ and radius, we believe that the cool companions can be BSSs and the hot companions can be WDs.

5. Blue Straggler Stars

5.1. Mass and Age Estimation of BSSs

The mass of the BSSs is critical for understanding their formation mechanisms. We constructed the H-R diagram of BSSs, which is shown in Figure 7. The Group 1 (blue) and Group 2 (red) BSSs are shown as filled circles. To determine

---

[9] http://svo2.cab.inta-csic.es/theory/vosa50/helpw4.php?otype=star&action=help&what=fitbin
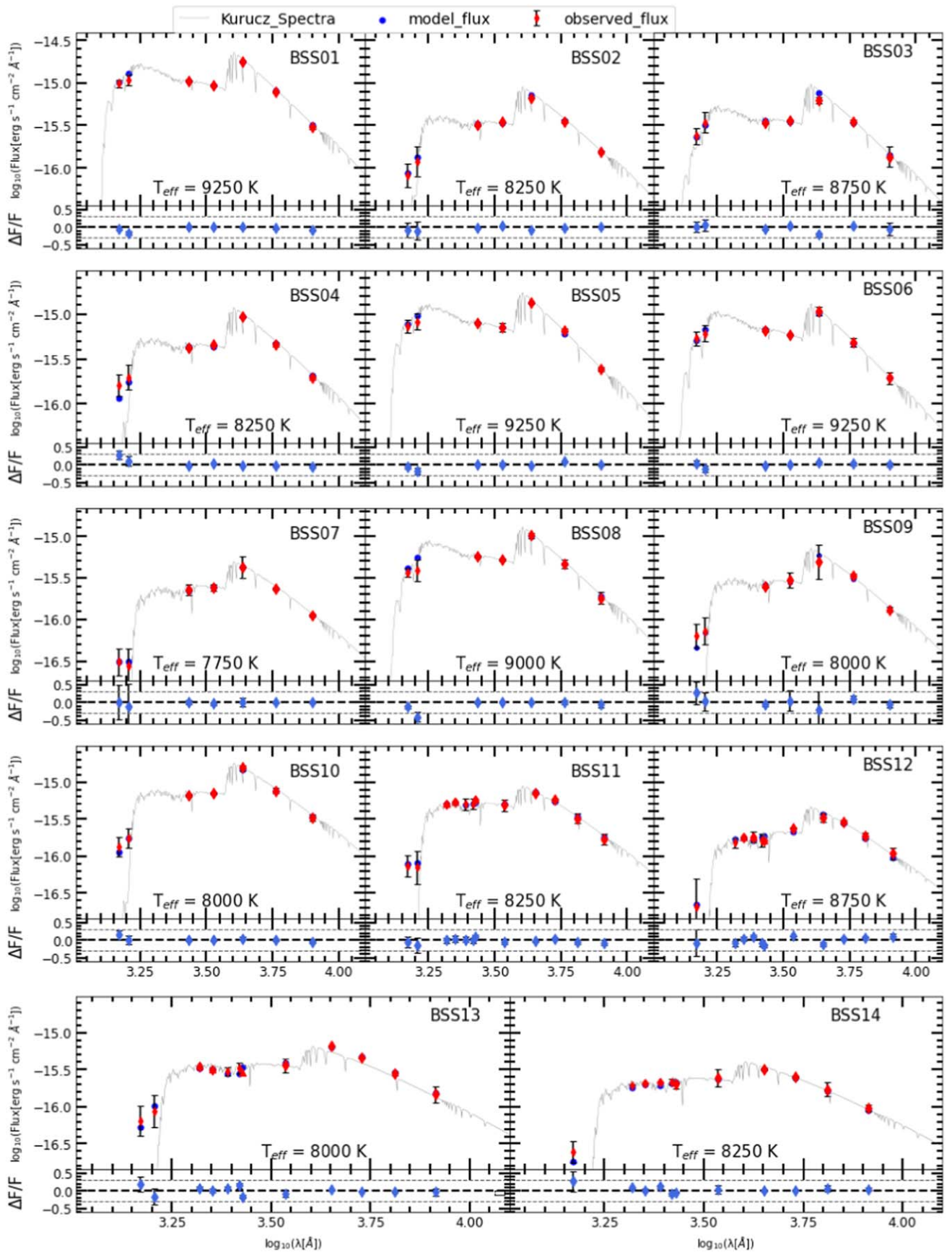
Figure 5. The SEDs of single-component BSSs. The blue filled circles represent the synthetic flux from the model used to fit the observed SED of single-component BSSs. The best-fit atmospheric parameters are mentioned in Table 2. The residuals of the SED fit are presented in the lower panel of all plots.
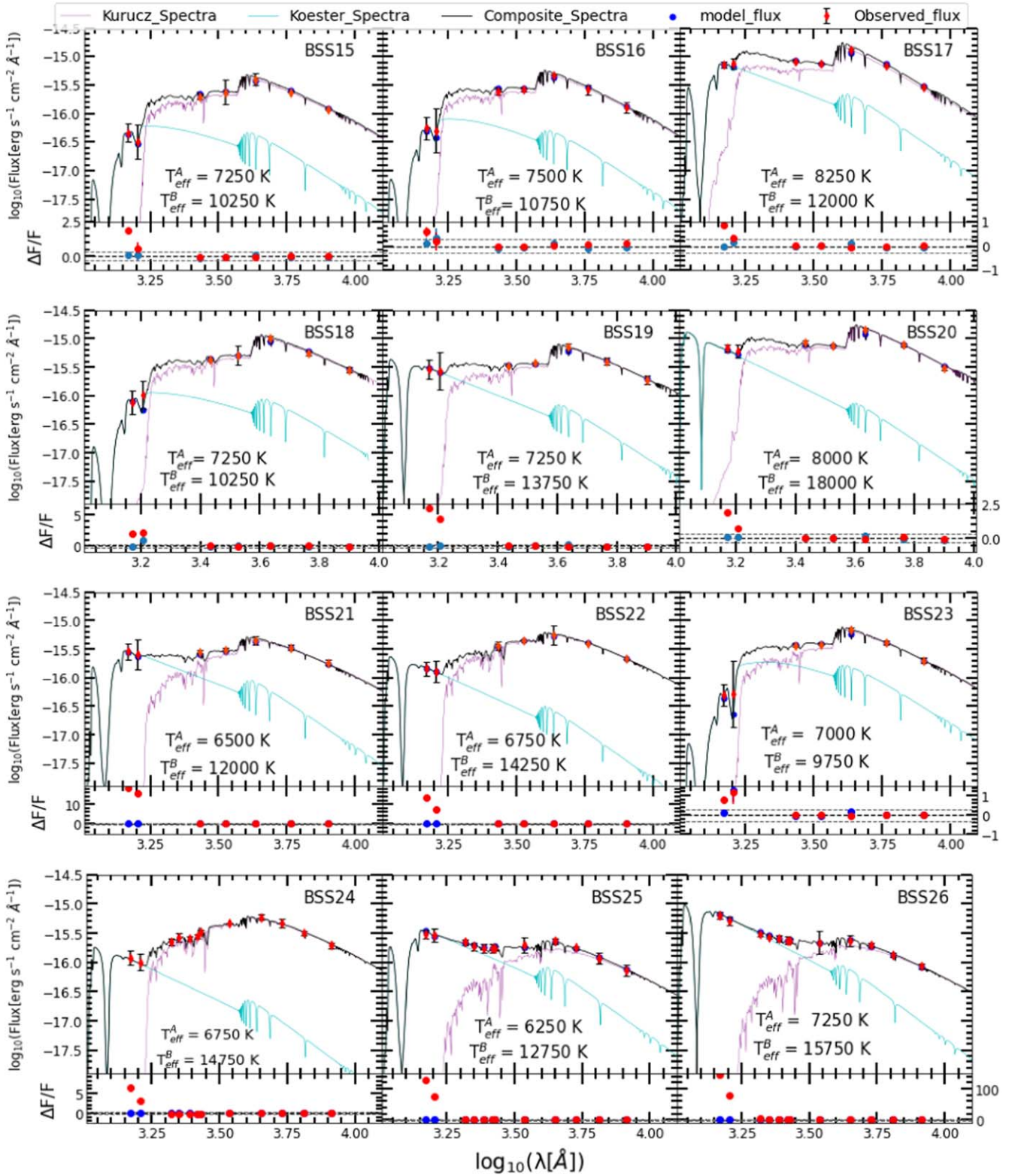
Figure 6. The SEDs of double-component BSSs using the data taken from UVIT, UVOT, and the 2.2 m ESO/MPI telescope after correcting for extinction. The composite SED fit to the BSSs is shown in black, while purple and cyan spectra represent the Kurucz and Koester models as displayed in the legend, respectively. The best-fit parameters are displayed in Table 3.

the mass of BSSs, we have plotted BaSTI evolutionary tracks (Hidalgo et al. 2018; Pietrinferni et al. 2021) depicted with solid lines in the H-R diagram as shown in Figure 7. The theoretical evolutionary tracks have ages ranging from 1 to 8.5 Gyr with 0.5 Gyr steps. The location of BSSs in the CMD suggests that they are more massive than typical GC stars. Their masses are calculated by comparing their positions with the overlaid tracks. The derived masses and ages of 26 BSSs are ~ 1.0–$1.6\,M_\odot$ and 1.5–8.5 Gyr, respectively.

Table 2
The Best-fit Parameters of Single-component BSSs

Name	R.A.	Decl.	T_{eff} (K)	log g	χ_r^2	$L/L_\odot$	$R/R_\odot$	Vgf	Vgf_b	N_{fit}/N_{tot}
BSS01	15.81374	−70.85611	9250^{+500}_{-250}	4.5	9.92	$19.140^{+0.170}_{-0.320}$	$1.718^{+0.100}_{-0.180}$	22.10	0.99	7/7
BSS02	15.81938	−70.84622	8250^{+250}_{-750}	4.0	10.60	$7.424^{+0.001}_{-0.299}$	$1.343^{+0.220}_{-0.073}$	5.65	0.66	7/7
BSS03	15.80834	−70.85098	8750^{+250}_{-1000}	4.0	7.24	$7.537^{+0.136}_{-0.219}$	$1.210^{+0.292}_{-0.104}$	23.60	1.48	7/7
BSS04	15.79833	−70.85612	8250^{+250}_{-750}	4.0	11.70	$9.847^{+0.313}_{-0.247}$	$1.541^{+0.368}_{-0.203}$	15.70	2.39	7/7
BSS05	15.81351	−70.84771	9250^{+500}_{-500}	4.5	13.70	$14.860^{+0.300}_{-0.030}$	$1.493^{+0.181}_{-0.133}$	15.70	1.03	7/7
BSS06	15.79856	−70.85527	9250^{+250}_{-500}	5.0	11.03	$11.690^{+0.680}_{-0.030}$	$1.325^{+0.255}_{-0.065}$	6.99	0.47	7/7
BSS07	15.81503	−70.84177	7750^{+500}_{-250}	4.5	4.92	$4.970^{+0.079}_{-0.030}$	$1.236^{+0.070}_{-0.121}$	3.73	3.01	7/7
BSS08	15.83265	−70.83091	9000^{+250}_{-500}	4.5	27.82	$10.740^{+0.370}_{-0.320}$	$1.356^{+0.239}_{-0.118}$	23.30	4.49	7/7
BSS09	15.81316	−70.83779	8000^{+250}_{-500}	4.0	10.22	$6.324^{+0.110}_{-0.358}$	$1.311^{+0.199}_{-0.163}$	10.20	2.54	7/7
BSS10	15.7891	−70.83161	8000^{+250}_{-500}	4.0	21.82	$15.920^{+0.160}_{-1.000}$	$2.074^{+0.296}_{-0.322}$	15.00	1.81	7/7
BSS11	15.82898	−70.81353	8000^{+250}_{-500}	5.0	27.24	$8.920^{+0.349}_{-0.307}$	$1.568^{+0.362}_{-0.100}$	18.40	3.99	11/12
BSS12	15.63451	−70.89542	8250^{+250}_{-500}	4.5	27.46	$7.756^{+0.539}_{-0.13}$	$1.371^{+0.367}_{-0.091}$	17.30	3.45	11/12
BSS13	15.65826	−70.81532	7500^{+250}_{-750}	4.0	23.94	$4.538^{+0.375}_{-0.097}$	$1.181^{+0.331}_{-0.092}$	18.50	1.53	11/12
BSS14	16.07722	−70.92675	7750^{+750}_{-250}	5.0	26.69	$4.369^{+0.124}_{-0.273}$	$1.151^{+0.107}_{-0.228}$	13.10	2.16	11/11

Note. The positions (R.A., decl.) are given in degrees. The T_{eff} is the effective temperature in K, log g is the surface gravity in logarithm unit, the reduced χ^2 (χ_r^2), the luminosity ($L/L_\odot$) and radius ($R/R_\odot$) are in solar units, Vgf and Vgf_b are the visual goodness of fit, N_{fit} is the number of points considered in the fitting, and N_{tot} is the total number of points.

We also note that the blue (Group 1) and red (Group 2) BSSs are found to occupy separate areas in the H-R diagram and could make two sequences. This is discussed below.

5.2. BSS Double Sequence

D13 discovered a double BSS sequence in NGC 362. On the basis of a comparison of the observed BSS distribution with theoretical models, they have suggested the presence of two parallel BSS sequences. They claim that the blue sequence is primarily formed by collisions, whereas the red sequence is formed through a continuous MT formation process. Based on our SED analysis, we classify Group 1 as single and Group 2 as binary BSSs. To compare the position of the Group 1 and Group 2 BSSs with the CMD of D13, we converted F606W ACS magnitude to F555W WFC3 magnitude using the equations given in Jang & Lee (2017). It is obvious that our Group 1 and Group 2 BSS locations in the CMD correspond to the blue and red groups of D13.

In Figure 8, we plotted Group 1 and 2 BSSs with blue and red filled circles, respectively. The blue curve represents a collisional isochrone of 0.2 Gyr age (Sills et al. 2009), while the orange curve represents the MT model. The blue line and orange box correspond to the same region defined by D13 for collisional and MT BSSs, respectively. This diagram shows that Group 1 BSSs adhere to the collisional model, whereas Group 2 BSSs occupy the region defined for the BSSs formed via MT. This is consistent with the conclusions made in D13. Therefore, we can say that Group 1 BSSs formed through collision, whereas Group 2 BSSs formed through MT. We found five FUV-bright BSSs brighter than 17 mag in this analysis, as shown in Figure 8. D13 did not identify these BSSs in their study. Figure 8 also suggests that these bright BSSs are following a blue and red sequence.

To check the temperature distribution of Group 1 and Group 2 BSSs, we created a histogram of effective temperature for all BSSs, as shown in Figure 9. Group 1 and 2 BSSs are represented by blue and red colors, respectively. Group 1 BSSs have a significantly higher temperature than Group 2 BSSs. This indicates that collisional BSSs have higher temperatures

as compared to MT BSSs. We did not perform the radial distribution of Group 1 and Group 2 BSSs because the number of FUV-bright BSSs was insufficient.

5.3. H-R Diagram

We already discussed the locations of the BSSs in the H-R diagram in Section 5.1. To study their properties, we overplotted the BaSTI isochrones and BaSTI ZAHB for the 11 Gyr age with black lines. The BSSs are clearly visible in this diagram at the extension part of the MS and beneath the ZAHB. The H-R diagram of hot companions of the Group 2 BSSs is shown in Figure 10. Along with the error bars, the hot companions are represented by cyan filled circles. The blue line represents the WD cooling curve for mass $0.5\,M_\odot$. This diagram shows that the hot companions are located between MS and WD cooling curves and are much less luminous than the HB stars. Based on the location of the hot companions in the H-R diagram, they could be ELM WDs. To determine the mass and cooling age of ELM WDs, we overplotted the ELM WD cooling curves (Istrate et al. 2016) in magenta for the mass range of 0.165–0.202 $M_\odot$. Using the closest ELM WD cooling curve, the cooling age and mass of individual ELM WDs can be estimated, and the same is listed in Table 4. Table 4 infers that the cooling age and mass range of ELM WDs are 200–1400 Myr and 0.164–0.202 $M_\odot$, respectively.

6. Discussion

We have identified 26 FUV-bright BSSs in NGC 362 based on the data taken from UVIT/AstroSat, HST, and Gaia eDR3. The BSSs are selected up to r_t of the cluster. In our analysis, 14 BSSs are found as single stars, and 12 BSSs have companions as ELM WDs. The BSSs and ELM WDs are characterized using the SEDs. Discussions on the findings are given below.

The SED analysis of 26 BSSs was carried out by fitting the Kurucz stellar atmospheric model. SED analysis revealed that 14 BSSs are single stars. We can deduce that they formed through a collisional process by comparing them to the model. However, three BSSs are located in the cluster's outskirts. The origin of the outer BSSs is unknown. Bolte et al. (1993) and

Table 3
The Best-fit Parameters for the Double-component BSSs

Name	R.A.	Decl.	$T_{\rm eff}$ (K)	log g	χ_r^2	$L/L_\odot$	$R/R_\odot$	Vgf	Vgf$_b$	$N_{\rm fit}/N_{\rm tot}$
BSS15 A	15.84851	−70.85769	7250^{+125}_{-125}	4.00	6.059	$4.543^{+0.045}_{-0.040}$	$1.353^{+0.010}_{-0.010}$	5.86	4.73	7/7
BSS15 B			10250^{+750}_{-250}	6.50	6.059	$0.393^{+0.078}_{-0.065}$	$0.199^{+0.029}_{-0.033}$	5.86	4.73	7/7
BSS16 A	15.83432	−70.85095	7500^{+125}_{-125}	4.00	1.415	$5.075^{+0.120}_{-0.164}$	$1.335^{+0.013}_{-0.024}$	1.25	0.91	7/7
BSS16 B			10750^{+500}_{-250}	7.25	1.415	$0.498^{+0.157}_{-0.098}$	$0.204^{+0.076}_{-0.036}$	1.25	0.91	7/7
BSS17 A	15.81471	−70.85065	8250^{+125}_{-125}	4.00	27.300	$12.790^{+0.080}_{-0.770}$	$1.753^{+0.005}_{-0.041}$	12.40	0.95	7/7
BSS17 B			12000^{+250}_{-1000}	7.25	27.300	$3.286^{+0.538}_{-0.095}$	$0.420^{+0.125}_{-0.023}$	12.40	0.95	7/7
BSS18 A	15.82657	−70.84255	7250^{+125}_{-125}	3.50	3.600	$10.800^{+0.160}_{-0.190}$	$2.086^{+0.009}_{-0.136}$	2.57	0.96	7/7
BSS18 B			10250^{+500}_{-250}	6.50	3.600	$0.877^{+0.121}_{-0.220}$	$0.298^{+0.034}_{-0.057}$	2.57	0.96	7/7
BSS19 A	15.80813	−70.84887	7250^{+125}_{-125}	3.50	13.760	$07.646^{+0.000}_{-0.900}$	$1.766^{+0.210}_{-0.008}$	9.17	1.75	7/7
BSS19 B			13750^{+750}_{-250}	6.50	13.760	$1.241^{+0.069}_{-0.050}$	$0.195^{+0.009}_{-0.023}$	9.17	1.75	7/7
BSS20 A	15.81073	−70.84724	8000^{+125}_{-125}	4.00	8.532	$14.910^{+0.220}_{-0.430}$	$2.040^{+0.007}_{-0.035}$	8.53	2.11	7/7
BSS20 B			18000^{+750}_{-750}	6.50	8.532	$2.149^{+0.321}_{-0.207}$	$0.151^{+0.085}_{-0.018}$	8.53	2.11	7/7
BSS21 A	15.80635	−70.84908	6500^{+125}_{-125}	3.50	6.984	$5.995^{+0.116}_{-0.151}$	$1.931^{+0.019}_{-0.014}$	4.85	1.12	7/7
BSS21 B			12000^{+500}_{-250}	7.00	6.984	$1.722^{+0.214}_{-0.001}$	$0.302^{+0.006}_{-0.032}$	4.85	1.12	7/7
BSS22 A	15.80396	−70.84564	6750^{+125}_{-125}	5.00	3.186	$8.032^{+0.190}_{-0.010}$	$2.046^{+0.009}_{-0.003}$	3.02	1.17	7/7
BSS22 B			14250^{+750}_{-250}	6.50	3.186	$0.614^{+0.076}_{-0.010}$	$0.127^{+0.001}_{-0.019}$	3.02	1.17	7/7
BSS23 A	15.80928	−70.8421	7000^{+125}_{-125}	3.50	9.313	$7.256^{+0.175}_{-0.199}$	$1.833^{+0.030}_{-0.097}$	5.94	2.75	7/7
BSS23 B			9750^{+500}_{-250}	6.75	9.313	$1.187^{+0.160}_{-0.109}$	$0.382^{+0.041}_{-0.082}$	5.94	2.75	7/7
BSS24 A	15.67558	−70.78341	6750^{+125}_{-125}	5.00	21.15	$08.157^{+0.100}_{-1.608}$	$2.112^{+0.004}_{-0.003}$	11.5	0.57	12/12
BSS24 B			14500^{+250}_{-1000}	6.50	21.15	$00.455^{+0.014}_{-0.015}$	$0.107^{+0.012}_{-0.001}$	11.5	0.57	12/12
BSS25 A	15.74852	−70.89148	6250^{+125}_{-125}	5.00	09.35	$02.331^{+0.038}_{-0.101}$	$1.308^{+0.012}_{-0.029}$	8.02	0.87	12/12
BSS25 B			12750^{+750}_{-250}	7.50	09.35	$01.376^{+0.026}_{-0.043}$	$0.241^{+0.028}_{-0.012}$	8.02	0.87	12/12
BSS26 A	15.69907	−70.82305	7250^{+125}_{-125}	5.00	26.45	$02.824^{+0.085}_{-0.055}$	$1.064^{+0.003}_{-0.011}$	17.1	1.12	12/12
BSS26 B			15750^{+250}_{-500}	7.75	26.45	$02.312^{+0.010}_{-0.132}$	$0.206^{+0.016}_{-0.093}$	17.1	1.12	12/12

Note. Headers are the same as described in Table 2. Here "A" denotes the cool component (BSS) and "B" denotes the hot component (ELM WD).
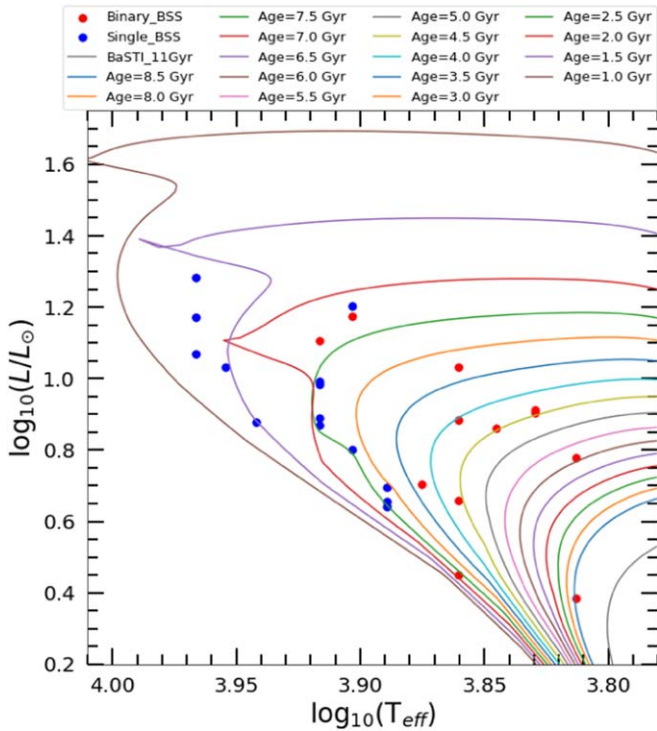

Figure 7. The H-R diagram ($L(L_\odot)$, $T_{\rm eff}$(K)) for 26 BSSs. The Group 1 and 2 BSSs are shown in blue and red, respectively. The theoretical isochrones taken from BaSTI (Hidalgo et al. 2018; Pietrinferni et al. 2021) for $[\alpha/{\rm Fe}] = 0.4$ are represented by the solid lines with a step of 0.5 Gyr in age.
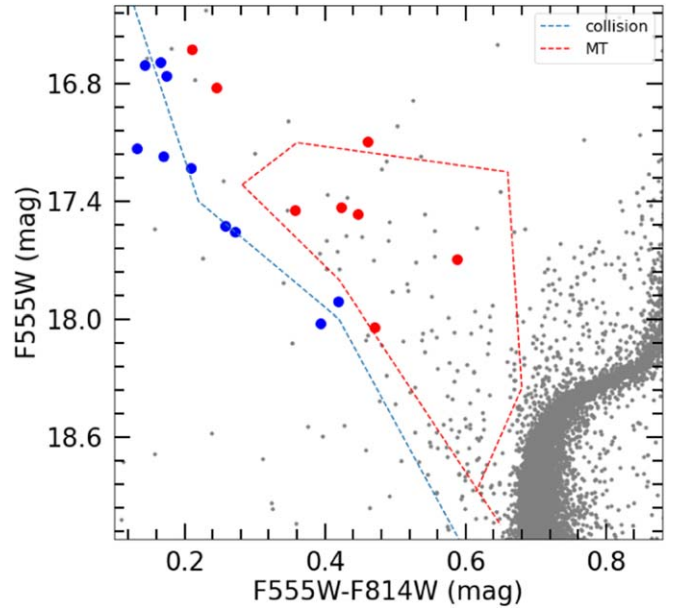

Figure 8. The F555W, (F555W − F814W) CMD for the FUV-bright BSSs. The Group 1 and 2 BSSs are plotted with red and blue points. The dotted blue line is a 0.2 Gyr collisional isochrone, and the red dotted box indicates the region of MT binaries taken from D13.

Sigurdsson et al. (1994) have suggested that the outer BSSs may have been formed by collisions during resonance encounters between binary and single stars in the core and ejected into the outer regions by the recoil from the interactions. On the other hand, Bailyn & Pinsonneault (1995) suggested that the outer BSSs have formed from mergers of primordial binaries, similar to the BSSs in sparse
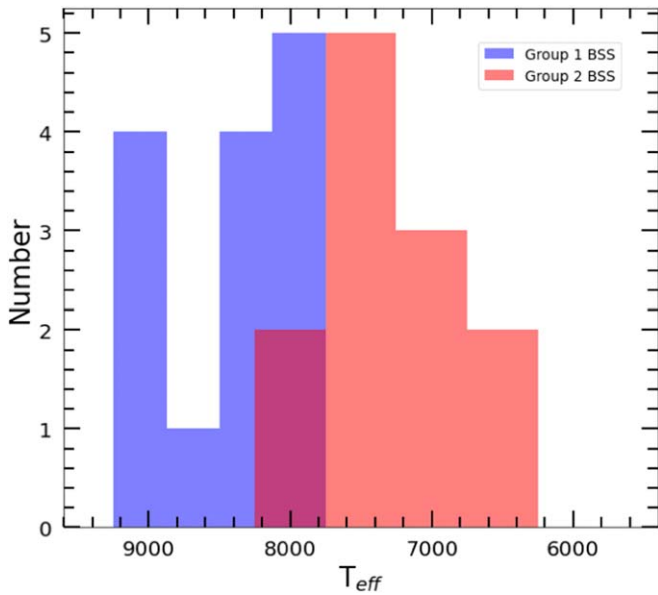
Figure 9. The number distribution of BSSs with effective temperature. The Group 1 and 2 BSSs are highlighted with blue and red, respectively.
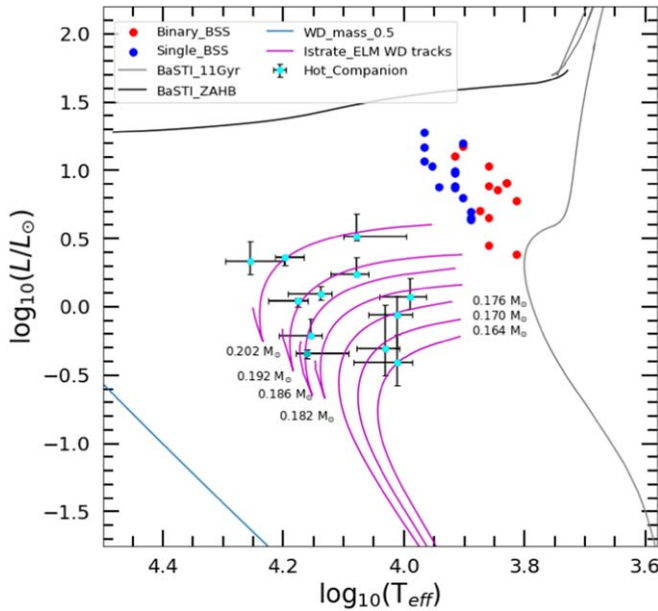

Figure 10. The H-R diagram with both BSSs (single-component BSSs, the cooler component of the two-component BSSs) represented as blue and red filled circles, respectively, and the hotter components of Group 2 denoted by cyan circles. The BaSTI isochrones and BaSTI ZAHB are depicted as a brown and black curve, respectively, with the cluster's age 11 Gyr. The ELM WD curves (Istrate et al. 2016) are plotted as magenta solid lines with masses 0.151–0.202 $M_\odot$.

Table 4
The Mass and Cooling Age (in Myr) for the ELMs

Name	Mass ($M_\odot$)	Cooling Age
BSS15 B	0.164–0.170	1285–1400
BSS16 B	0.170–0.176	480–580
BSS18 B	0.176–0.182	1285–1400
BSS23 B	0.182–0.186	755–875
BSS22 B, BSS24 B	0.186–0.192	460–475
BSS19 B, BSS21 B, BSS25 B	0.192–0.202	300–500
BSS17 B, BSS20 B, BSS26 B	0.202	200–400

clusters. To know a clear picture of the formation of outer BSSs, both of these explanations require elaboration. Both mechanisms appear to play an important role in the formation of outer BSSs in NGC 362.

In Section 5.1, we estimated the mass of each BSS. The highest mass of a BSS fitted through a single SED is 1.64 $M_\odot$. Furthermore, by comparing with the model in Section 5.2, we demonstrated that these BSSs formed via the collisional process. Assuming that the initial mass of the two BSS progenitor stars is the same as the cluster's turnoff mass (0.8 $M_\odot$), these two stars may collide and merge to form the cluster's highest-mass BSS.

A total of 12 out of 26 BSSs were identified as binary systems using the SEDs. The cool and hot components of the binary system were characterized by the Kurucz and Koester models. The physical properties derived in this analysis for the hot components indicate that they could be ELM WDs. We note that the Group 1 BSSs are found to have ages of ∼1.5 and ∼2.5 Gyr as seen from Figure 7. The BSS+ELM pairs are younger than the younger subgroup of the Group 1 BSSs.

We discovered that BSSs fitted with a double-component model have ELM WDs as companions in this study. The mass of a WD produced by a single star is limited to 0.4 $M_\odot$ (Brown et al. 2010). The age of the universe is also a limiting factor at the lower end of the WD mass. ELMs, on the other hand, can be found in binary form in the universe (Jadhav et al. 2019; Ratzloff et al. 2019, Subramaniam et al. 2020; Vaidya et al. 2022). The lower limit on the mass of the ELM WD can be attributed to mass loss during the early stages of evolution. The case A/B MT may result in the He core WD via early envelope mass loss (Iben 1991; Marsh et al. 1995). Therefore, MT is essential for the creation of ELM WDs in tight binary systems where the companion tears away the ELM WD progenitor's envelope and the low-mass core fails to ignite the He core. The companion star gained mass and converted to a BSS during the mass loss.

The mass range of detected ELM WDs is 0.16–0.20 $M_\odot$. According to Althaus et al. (2021), the mass threshold for the occurrence of CNO flashes on the cooling branch of ELM WDs is 0.2 $M_\odot$. Therefore, no ELM WDs detected in the current study should produce a CNO flash on the cooling branch. According to Li et al. (2019), ELM WDs with masses less than 0.22 $M_\odot$ formed from the RL overflow channel. We further conclude that these BSSs are formed via MT with an ELM WD as their companion.

In the present analysis, the maximum and minimum masses of the BSSs formed through the MT channel are 1.40 and 1.02 $M_\odot$, respectively. By assuming that the initial mass of the BSS progenitor is the same as the cluster's turnoff mass (0.8 $M_\odot$), the highest and lowest masses acquired by BSSs from the binary system's primary are 0.6 and 0.2 $M_\odot$, respectively. It is possible to acquire the lower limit of mass through an efficient case B MT, whereas the higher limit demands that the progenitor of the ELM be more massive than the turnoff mass so that more mass is available for transfer, or the present BSS went through more than one event of mass acquisition to gain up to 0.6 $M_\odot$.

The implication of finding the BSS+ELM WD pairs in a GC would be that these binary systems remained dynamically stable to complete the MT process. The cooling age of the ELM WDs suggests that they can be as young as 200 Myr and as old as 1.4 Gyr, where nine of them are younger than

~500 Myr. This cluster is understood to have undergone core collapse 200 Myr ago (Cadelano et al. 2022). If we assume that this cluster is a post-core-collapse cluster, then it is possible that the cluster experienced an increase in the number of binaries as a result of the core collapse. We speculate that these systems may be the result of the evolution of such binaries, as the cooling ages of the ELM WD companions and the time of core collapse are not very different.

Kamlah et al. (2022) found that in all of their simulations the overall WD binary fraction, as well as the WD−MS binary fraction, increases over a timescale of 10 Gyr. They also find that a good number of helium WDs are produced in their simulations, which can be formed only in binaries. They speculate that more frequent dynamical interactions force binaries to form helium WDs because of MT. The number of BSSs also increases with time, in their simulations. These ELM WDs, which are indeed helium WDs, as companions to BSSs are the first observational detections of such systems found in simulations. It is quite possible that we have detected probably the brightest of the ELM WDs and many more may be present.

Therefore, the post-MT binary systems (BSS+ELM WDs) could be formed as a result of either core collapse or the overall gradual dynamical evolution of the cluster. Either way, the detections of the BSSs with ELM WD companions found in this core-collapsed cluster have implications to constrain the dynamical evolution theories of GCs.

We do not attempt to study the radial distribution of these systems, as our data are incomplete in the central regions. In order to increase the sample of FUV-detected BSSs, we plan to carry out deeper observations of this cluster using UVIT for possible detection of fainter WD companions to BSSs.

7. Summary and Conclusions

In this work, we present the first detection of 12 BSSs with ELM WD companions in the GC NGC 362. The analysis is based on the UVIT observations, as well as archival data from UVOT, Gaia eDR3, and the 2.2 m ESO/MPI telescope. The following are the main findings of this study:

1. We have identified 26 FUV-bright BSSs, which are confirmed PM members, utilizing the UVIT and Gaia eDR3 data.
2. The stellar parameters of the FUV-bright BSSs were derived using the SED fitting technique. Out of 26 BSSs, 14 have been successfully fitted with a single-temperature SED. The effective temperature, radius, and luminosity of the 14 BSSs are in the range of $7500-9250$ K, $1.1-2.0 R_{\odot}$, and $4.3-19.1 L_{\odot}$, respectively.
3. A total of 12 BSSs were found to exhibit UV excess. The UV excess was more than 30% compared to the model. Therefore, a double-component SED was fitted to these BSSs, and ranges in stellar parameters ($T_{\rm eff} = 9750 -18,000$ K, $R = 0.1-0.4 R_{\odot}$, and $L = 0.4-3.3 L_{\odot}$) for the hot components (ELM WDs) were estimated. The cool component's (BSSs) temperature, radius, and luminosity were estimated to be $T_{\rm eff} = 6250-8250$ K, $R = 1.0-2.1 R_{\odot}$, and $L = 2.3-14.9 L_{\odot}$.
4. The masses of the hot components were found to be $0.16 - 0.20 M_{\odot}$. We classify the hot components as ELM WDs based on their location in the H-R diagram. For the first time in a GC, we detect ELM WDs as companions to BSSs formed via the case A/B MT pathway.

5. The mass of the BSSs was determined in the range of $1.0-1.6 M_{\odot}$ using the evolutionary tracks. We identified the double BSS sequence in the H-R diagram based on the SED analysis. In comparison to the model, our estimates support that the hotter BSSs are formed via a collisional process, whereas the cooler BSSs are formed via an MT pathway.
6. The cooling ages of nine of the ELM WD companions were estimated to be younger than 500 Myr, whereas this cluster is expected to have undergone core collapse ~200 Myr ago. These binary BSSs may be formed during the core collapse or as part of the dynamical evolution of the cluster. The detections of these post-MT systems in this core-collapsed cluster therefore provide new constraints on its internal dynamics.

ORCID iDs

Arvind K. Dattatrey ⓘ https://orcid.org/0000-0002-4729-9316
Sharmila Rani ⓘ https://orcid.org/0000-0003-4233-3180
Annapurni Subramaniam ⓘ https://orcid.org/0000-0003-4612-620X

References

Althaus, L. G., Gil-Pons, P., Córsico, A. H., et al. 2021, A&A, 646, A30
Althaus, L. G., Miller Bertolami, M. M., & Córsico, A. H. 2013, A&A, 557, A19
Anderson, J., Bedin, L. R., Piotto, G., Yadav, R. S., & Bellini, A. 2006, A&A, 454, 1029
Bailyn, C. D., & Pinsonneault, M. H. 1995, ApJ, 439, 705
Baumgardt, H. 2017, MNRAS, 464, 2174
Beccari, G., Ferraro, F. R., Dalessandro, E., et al. 2019, ApJ, 876, 87
Bolte, M., Hesser, J. E., & Stetson, P. B. 1993, ApJL, 408, L89
Brown, W. R., Kilic, M., Allende Prieto, C., & Kenyon, S. J. 2010, ApJ, 723, 1072
Cadelano, M., Ferraro, F. R., Dalessandro, E., et al. 2022, ApJ, 941, 69
Castelli, F., Gratton, R. G., & Kurucz, R. L. 1997, A&A, 318, 841
Castelli, F., & Kurucz, R. L. 2003, in Modeling of Stellar Atmospheres, Proc. of the 210th Symp. of the IAU, ed. N. Piskunov et al. (San Francisco, CA: ASP), A20
Chen, Y., Girardi, L., Fu, X., et al. 2019, A&A, 632, A105
Clarkson, W. I., Sahu, K. C., Anderson, J., et al. 2011, ApJ, 735, 37
Dalessandro, E., Ferraro, F. R., Massari, D., et al. 2013, ApJ, 778, 135
Ferraro, F. R., Beccari, G., Dalessandro, E., et al. 2009, Natur, 462, 1028
Ferraro, F. R., D'Amico, N., Possenti, A., Mignani, R. P., & Paltrinieri, B. 2001, ApJ, 561, 337
Ferraro, F. R., Lanzoni, B., Raso, S., et al. 2018, ApJ, 860, 36
Ferraro, F. R., Pecci, F. F., Cacciari, C., et al. 1993, AJ, 106, 2324
Fitzpatrick, E. L. 1999, PASP, 111, 63
Harris, W. E. 2010, arXiv:1012.3224
Hidalgo, S. L., Pietrinferni, A., Cassisi, S., et al. 2018, ApJ, 856, 125
Hills, J. G., & Day, C. A. 1976, ApJL, 17, 87
Iben, I. J. 1991, ApJS, 76, 55
Indebetouw, R., Mathis, J. S., Babler, B. L., et al. 2005, ApJ, 619, 931
Istrate, A. G., Marchant, P., Tauris, T. M., et al. 2016, A&A, 595, A35
Jadhav, V. V., Pandey, S., Subramaniam, A., & Sagar, R. 2021, JApA, 42, 89
Jadhav, V. V., Sindhu, N., & Subramaniam, A. 2019, ApJ, 886, 13
Jang, I. S., & Lee, M. G. 2017, ApJ, 835, 28
Jiménez-Esteban, F. M., Torres, S., Rebassa-Mansergas, A., et al. 2018, MNRAS, 480, 4505
Johnson, H. L., & Sandage, A. R. 1955, ApJ, 121, 616
Kamlah, A. W. H., Leveque, A., Spurzem, R., et al. 2022, MNRAS, 511, 4060

Kilic, M., Brown, W. R., Allende Prieto, C., Pinsonneault, M. H., & Kenyon, S. J. 2007, ApJ, 664, 1088

Kippenhahn, R., Weigert, A., & Hofmeister, E. 1967, MComP, 7, 129

Koester, D. 2010, Mem. Soc. Astron. Italiana, 81, 921

Kravtsov, V., Dib, S., Calderón, F. A., & Belinchón, J. A. 2022, MNRAS, 512, 2936

Lanzoni, B., Sanna, N., Ferraro, F. R., et al. 2007, ApJ, 663, 1040

Leonard, P. J. T. 1989, AJ, 98, 217

Li, Z., Chen, X., Chen, H.-L., & Han, Z. 2019, ApJ, 871, 148

Marsh, T. R., Dhillon, V. S., & Duck, S. R. 1995, MNRAS, 275, 828

Martinazzi, E., Pieres, A., Kepler, S. O., et al. 2014, MNRAS, 442, 3105

Maxted, P. F. L., Bloemen, S., Heber, U., et al. 2014, MNRAS, 437, 1681

McCrea, W. H. 1964, MNRAS, 128, 147

Meylan, G., & Heggie, D. C. 1997, A&AR, 8, 1

Nardiello, D., Libralato, M., Piotto, G., et al. 2018, MNRAS, 481, 3382

Paczyński, B. 1971, ARA&A, 9, 183

Pandey, S., Subramaniam, A., & Jadhav, V. V. 2021, MNRAS, 507, 2373

Perets, H. B., & Fabrycky, D. C. 2009, ApJ, 697, 1048

Pietrinferni, A., Hidalgo, S., Cassisi, S., et al. 2021, ApJ, 908, 102

Portegies Zwart, S., & Leigh, N. W. C. 2019, ApJL, 876, L33

Postma, J. E., & Leahy, D. 2017, PASP, 129, 981

Preston, G. W., & Sneden, C. 2000, AJ, 120, 1014

Rani, S., Pandey, G., Subramaniam, A., Sahu, S., & Rao, N. K. 2021, MNRAS, 501, 2140

Raso, S., Ferraro, F. R., Dalessandro, E., et al. 2017, ApJ, 839, 64

Ratzloff, J. K., Barlow, B. N., Kupfer, T., et al. 2019, ApJ, 883, 51

Rebassa-Mansergas, A., Solano, E., Jiménez-Esteban, F. M., et al. 2021, MNRAS, 506, 5201

Renzini, A., & Fusi Pecci, F. 1988, ARA&A, 26, 199

Rivera-Sandoval, L. E., van den Berg, M., Heinke, C. O., et al. 2015, MNRAS, 453, 2707

Rodrigo, C., Solano, E., Bayo, A., Cortés-Contreras, M., & Jiménez-Esteban, F. 2019, in Highlights on Spanish Astrophysics X: Proc. of the XIII Scientific Meeting of the Spanish Astronomical Society, ed. B. Montesinos et al. (Spain: Spanish Astronomical Society), 430

Sahu, S., Subramaniam, A., Singh, G., et al. 2022, MNRAS, 514, 1122

Sandage, A. R. 1953, AJ, 58, 61

Shara, M. M., Saffer, R. A., & Livio, M. 1997, ApJL, 489, L59

Siegel, M. H., Porterfield, B. L., Linevsky, J. S., et al. 2014, AJ, 148, 131

Sigurdsson, S., Davies, M. B., & Bolte, M. 1994, ApJL, 431, L115

Sills, A., Karakas, A., & Lattanzio, J. 2009, ApJ, 692, 1411

Simunovic, M., Puzia, T. H., & Sills, A. 2014, ApJL, 795, L10

Sindhu, N., Subramaniam, A., Jadhav, V. V., et al. 2019, ApJ, 882, 43

Singh, G., Sahu, S., Subramaniam, A., & Yadav, R. K. S. 2020, ApJ, 905, 44

Singh, G., & Yadav, R. K. S. 2018, MNRAS, 482, 4874

Stetson, P. B. 1987, PASP, 99, 191

Stetson, P. B., Pancino, E., Zocchi, A., Sanna, N., & Monelli, M. 2019, MNRAS, 485, 3042

Subramaniam, A., Pandey, S., Jadhav, V. V., & Sahu, S. 2020, JApA, 41, 45

Subramaniam, A., Sindhu, N., Tandon, S. N., et al. 2016a, ApJL, 833, L27

Subramaniam, A., Tandon, S. N., Hutchings, J., et al. 2016b, Proc. SPIE, 9905, 99051F

Tandon, S. N., Subramaniam, A., Girish, V., et al. 2017, AJ, 154, 128

Vaidya, K., Panthi, A., Agarwal, M., et al. 2022, MNRAS, 511, 2274

van Kerkwijk, M. H., Bassa, C. G., Jacoby, B. A., & Jonker, P. G. 2005, ASP Conf. Ser. 328, Binary Radio Pulsars, ed. F. A. Rasio & I. H. Stairs,, 357, arXiv:astro-ph/0405283

Vasiliev, E., & Baumgardt, H. 2021, MNRAS, 505, 5978

Zinn, R., & Searle, L. 1976, ApJ, 209, 734